

# Simulation Analysis of Stellite 6<sup>®</sup> Particle Impact on Steel Substrate in Supersonic Laser Deposition Process

Fang Luo, Andrew Cockburn, Dingbao Cai, Martin Sparks, Yuanhang Lu, Cairong Ding, Richard Langford, William O'Neill, Jianhua Yao, and Rong Liu

(Submitted March 24, 2014; in revised form September 2, 2014)

The particle impact behavior of Stellite 6 on steel substrate in the supersonic laser deposition (SLD) process is studied using numerical simulation, compared with experimental data. The impact characteristics of Stellite 6 are analyzed with respect to particle size and deposition temperature. The simulation results show that laser deposition temperature of 1000 °C for the substrate is the optimal in terms of the interface bonding between the particles and substrate. The particle size of 40 μm exhibits the best deposition interface. The simulation results agree well with the experimental measurements. The depths of impact indentation with different particle sizes and at different temperatures are investigated to obtain the relationships between process parameters such as particle diameter, indentation depth, and deposition temperature. To further understand the effects of collisional behavior of multi-particles on the stress-strain distributions and the micro-zone in the particle and substrate system, different micro-zones of the impact particle are analyzed; the variations of the stress and strain with time for the substrate and particle are obtained from the simulation results. The impact characteristics of Stellite 6 deposited on steel substrate are discussed.

**Keywords** impact characteristics, simulation, Stellite 6, supersonic laser deposition

## 1. Introduction

Supersonic laser deposition (SLD), that combines the supersonic powder stream generated in cold spray (CS) with laser heating of the deposition zone, is a novel coating fabrication process. This technique takes advantages of CS and laser, and overcomes the drawback of the

cold spraying technology that it cannot deposit brittle materials and high hardness materials such as ceramic, Ni60, and Stellite 6 (St 6). (Ref 1), and low deposition efficiency of laser. SLD has attracted much attention of researchers due to using nitrogen to replace helium for reducing cost and achieving high-quality deposition for hard materials such as titanium (Ref 2), St 6, or carbides (Ref 3). Traditionally, these hard particles can only be deposited using a gas with a high speed of sound (e.g., helium), making the process prohibitively expensive.

Many of the experimental results in various aspects of CS particle impact research have been reported in recent years (Ref 4–8), such as critical particle velocity and particle size and effective deposition efficiency. However, these findings cannot completely explain the phenomena observed in the CS process, for instance, the characteristics of interface between particles and substrate during impact, etc. The behavior of particle impact on the substrate has also been studied using numerical simulation in combination with experiments and theory analysis (Ref 9–15). The results demonstrated that cold spray characteristics and the created interface bonding strength can be attributed to adiabatic shear instabilities which occur at the particle surface at or beyond the critical velocity, etc. (Ref 9, 10). For spherical copper powder with low oxygen content, the critical velocity was determined to be about 570 m/s, with nitrogen as the process gas and particle grain sizes 5–25 μm, deposition efficiencies over 70% were achieved. With increasing particle velocity, two critical velocities were concerned. One was for particle deposition onto the substrate and the other for particle-particle bonding (Ref 11). For example, for Al-Si feed-

**Fang Luo**, College of Zhijiang, Zhejiang University of Technology, Hangzhou 310024, Zhejiang, China and Key Laboratory of Special Purpose Equipment and Advanced Processing Technology (Zhejiang University of Technology), Ministry of Education, Hangzhou 310014, Zhejiang, China; **Andrew Cockburn, Martin Sparks, and William O'Neill**, Institute for Manufacturing, Department of Engineering, University of Cambridge, Cambridge CB3 0FS, UK; **Dingbao Cai**, College of Economics and Management, Zhejiang University of Technology, Hangzhou 310024, Zhejiang, China; **Yuanhang Lu and Jianhua Yao**, Key Laboratory of Special Purpose Equipment and Advanced Processing Technology (Zhejiang University of Technology), Ministry of Education, Hangzhou 310014, Zhejiang, China; **Cairong Ding**, State Key Laboratory of Optoelectronic Materials and Technologies, Sun Yat-Sen University, Guangzhou, 510275, Guangdong, China; **Richard Langford**, Cavendish Laboratory, University of Cambridge, Cambridge CB3 0FS, UK; and **Rong Liu**, Department of Mechanical & Aerospace Engineering, Carleton University, 1125 Colonel By Drive, Ottawa, ON K1S 5B6, Canada. Contact e-mails: luofang@zjut.edu.cn and Rong.Liu@carleton.ca.

stock coating onto mild steel substrate, the particles were more easily bonded to the substrate than to each other. When the mean particle size was 25  $\mu\text{m}$ , the two critical velocities were measured to be 580 and 700 m/s, respectively. The deposition efficiency (DE) value increased with the mean particle velocity and the maximum DE was about 37% at a mean particle velocity of 800 m/s. The substrate surface roughness did not affect the DE significantly. The maximum particle velocity was obtained from the optimum gas conditions of 2.9 MPa and 500  $^{\circ}\text{C}$  (Ref 14). Cu-Sn alloy feedstock was deposited onto aluminum, mild steel, and bronze substrates. The experimental results showed that the critical velocity decreased by 50 m/s when the process gas temperature was increased by 100  $^{\circ}\text{C}$ . The difference between the critical velocity for particle deposition onto aluminum substrate ( $V_{cr1}$ ) and for particle-particle bonding ( $V_{cr2}$ ); the latter (330 m/s) was higher than the former (160 m/s) (Ref 15). The bonding strength at the substrate/coating interface mainly depended on the first stage critical velocity. For irregular shape particles, the in-flight velocity decreased from 390 to 282 m/s as the particle size increased from 20 to 60  $\mu\text{m}$ . The critical velocities for feedstock copper powder with spherical and irregular shape morphology were investigated to be 425 m/s and 550 m/s, respectively. For irregular shape particles, the critical velocity decreased from 550 to 460 m/s after preheated at 390  $^{\circ}\text{C}$  for 1 h. It was also found that the larger size powders led to a lower critical velocity (Ref 16).

In general, particle velocity prior to the impact is an important factor for CS because the successful deposition of cold-sprayed particles relies only on the kinetic energy rather than the combined effect of kinetic and thermal energies available in conventional thermal spraying. As for the bonding mechanism, some researchers (Ref 17-20) investigated the thermal softening zone using numerical and experimental methods. Considering the possible serious oxidation of the cold-sprayed particles under high-temperature conditions, the preheating temperature was limited to 300  $^{\circ}\text{C}$  for each test. The cold spray process usually involves preheating particle and increasing particle impact velocity to improve the deposition efficiency. The thermal softening effect of the interfacial layer and the relationship between particle size and deformation of cold spray were studied by King et al. (Ref 21, 22). The results showed that at the interface between cold-sprayed Ti particles and Ti substrate surface, voids existed due to nanometer-scale mismatch in surface topologies. These voids were eliminated over a linear fraction of 26-77% of the interface by plastic flow during impact deformation, making the interface 'melled.' Void closure was found more likely at the particle peripheries, and rarely inside the particles. Flattening of aluminum and copper particles cold-sprayed onto ceramic surfaces was described by an ellipsoidal function. It was shown that aluminum particle deformation was limited below  $\sim 5 \mu\text{m}$ , and copper deformation below  $\sim 2 \mu\text{m}$ . For hard particles, such as St 6, the deformation behavior of these particles deposited on steel substrate was never studied using simulation. SLD is a novel deposition technology. The deformation behavior of the high-speed St 6 particles in the SLD process is more

complex, compared to that in the CS process. When collision occurs, it cannot be observed directly in the coating deposition experiment; therefore, simulation analysis is necessary for SLD study, which can model the experimental process, save experimental cost, and manpower.

In this research, using the SLD technique St 6 powder was deposited onto mild steel experimentally (Ref 23); the deposition process was simulated using finite element analysis (FEA), with focus on investigating the impact characteristics of St 6 particle on steel surface, analyzing the variations of the stress, the strain, and impact depth in the coating layer, and obtaining the curve fitting relationships between the depth, particle diameter, and temperature using Matlab software.

## 2. Experiment and Simulation

### 2.1 Coating Material

St 6<sup>®</sup> is a cobalt-base alloy consisting of various carbides distributed in a solid solution matrix. Its chemical composition is given in Table 1. Figure 1 shows the topography and the distribution of the sphere particles used in this research. They have the diameter between 28 and 56  $\mu\text{m}$  and  $d(0.5)$  is 39.705.

### 2.2 Coating Fabrication

St 6 powder was deposited on carbon steel substrate using a SLD system (Ref 2). The sketch of the system setup is shown in Fig. 2. Its processing range is 500  $\times$  500  $\times$  300 mm. Processing conditions such as max traverse speed, torque rotary, max coil temperature, and N<sub>2</sub> line max pressure, are 300 mm/s, 750 rpm, 800  $^{\circ}\text{C}$ , and 35 bar, respectively. Selecting IPG system with 4 kW; the temperature control was achieved by Pyrometer Kleiber KMGALO, the powder feeding was implemented by the Praxair 1264 HP powder feeder. The spray distance from injection point was 270 mm; spray nozzle dimension was 6.06 mm/19 mm. Initially, single track was sprayed under a range of operating conditions to find the temperature range required for the deposition. To quickly identify an appropriate process, the operating pressure was maintained at 30 bar to give particle velocity about 35 g/min and traverse rate of 10 mm/s. The parameters concerned were deposition site temperature and N<sub>2</sub> temperature. The substrate specimens were machined to the dimension approximately 160  $\times$  55  $\times$  2 mm. The process parameters used to produce the St 6 coating specimen are given in Table 2. For multiple tracks, the optimal deposition site temperature and N<sub>2</sub> temperature were obtained from analyzing the single track coatings in surface topography, microstructure, hardness, and wear resistance. These temperatures along with other process parameters are reported in Table 3.

**Table 1 Chemical composition of St 6 powder**

Element	Co	W	Cr	C	Ni	Mo	Fe	Si	Others
wt. %	Bal.	5.65	28.63	1.24	<2.0	<1.0	<2.0	<2.0	<1.0

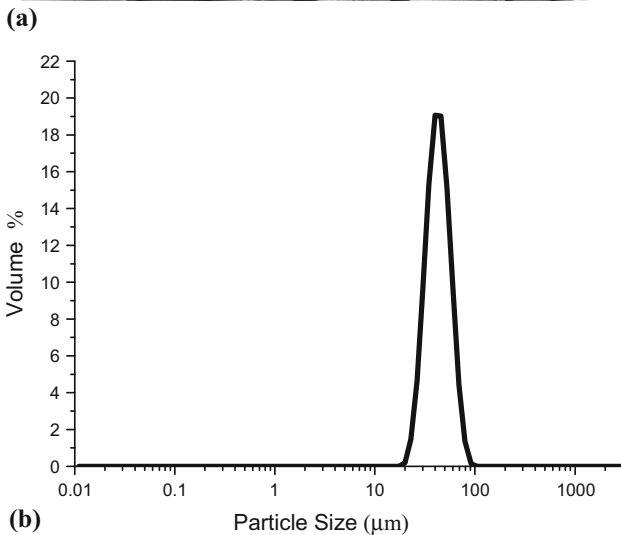
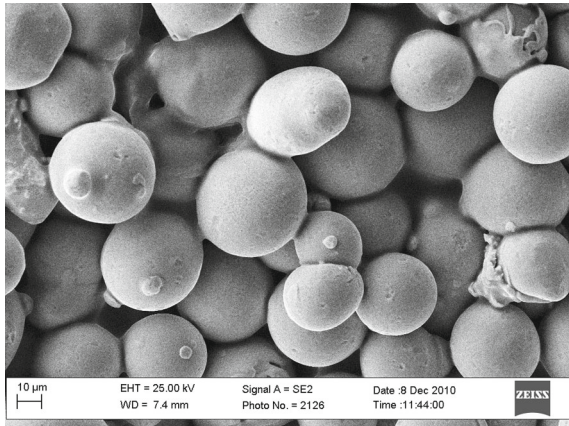


**Fig. 1** St 6 particles. (a) SEM image of morphology. (b) Distribution of particle sizes

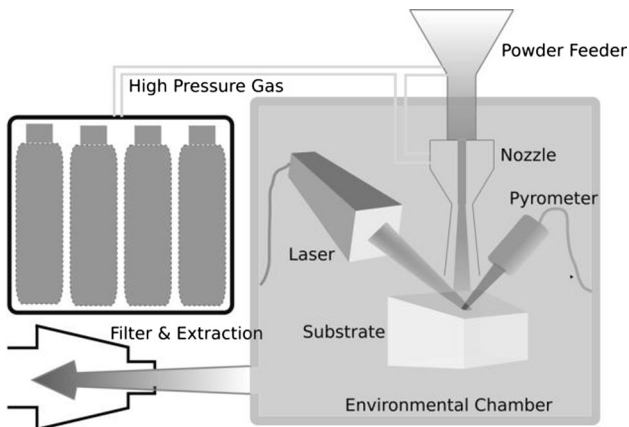


**Fig. 2** Schematic showing of the SLD system

### 2.3 Mathematical Model with Lagrangian Meshing

The impact behavior of copper particles on copper substrate was studied using the Johnson-Cook plasticity model with an explicit program LS-DYNA (Ref 7, 8). This

**Table 2** Process parameters of single track using SLD

Specimen	Parameter			
	N <sub>2</sub> pressure, bar	N <sub>2</sub> temperature, °C	Deposition site temperature, °C	Traverse rate, mm/s
1	30	450	500	10
2	30	450	1000	10
3	30	450	1100	10
4	30	450	1200	10

**Table 3** Optimal process parameters of multiple tracks using SLD

N <sub>2</sub> temperature, °C	N <sub>2</sub> pressure, bar	Laser power, kW	Traverse rate, mm/s	Deposition site temperature, °C
450	30	1.5	10	1000

model requires input of some constants, such as hardening coefficient  $B$  MPa, strain hardening exponent  $N$ , strain rate constant  $C$ , and softening exponent  $M$ , while these constants must be determined from experimental measurements. Since these constants for St 6 are not available whether from the alloy company or in literature, using the similar concepts, the impact behavior of St 6 particles deposited on carbon steel was simulated using the software package ANSYS Multiphysics/LS-DYNA (Ref 24, 25); Due to the fact that Eulerian method is difficult to track the deformation process of the coating material, thus cannot distinguish the interface between the particle and the substrate; therefore, this method is unable to describe the interface behavior between different materials when the particle material and the substrate material are not identical. In addition, using this method, finer meshing would cause the increase in calculation time and thus running cost (Ref 26); therefore, Lagrange algorithm was adopted in the discrete calculation. In order to demonstrate the interacting effects between the particles and substrate, three St 6 particles were concerned as the research unit. Assuming that the process of the particles with high impacting speeds is mainly controlled by the high-pressure gases, inertial force, gravity force, and other bulk forces could be neglected. To reduce element number and save calculation time, the 3D model was simplified as a quarter of symmetric model, with the size of the substrate  $4 \times 4$  mm, the radius of the particles  $20 \mu\text{m}$ , as shown in Fig. 3. To ensure the calculation accuracy of the deformation area, the size of the collision zone is  $40 \times 90 \times 60 \mu\text{m}$ , and the meshing size of the collision zone is  $3 \times 3 \times 3 \mu\text{m}$ .

### 2.4 Material Model

During the deposition process, St 6 particles and carbon steel substrate experience elastic-plastic deformation, therefore, elasticity and plasticity are described as the bilinearity of elasticity modulus and plasticity modulus; two kinds of gradient are used to express the strain and

stress characteristics of materials. Due to heat diffusion, temperature gradient is induced in the area of laser heating; the heated zone in both particles and substrate exhibit deformation behavior at six different temperatures, that is, from room temperature of 25 to 1100 °C. This temperature range is divided into six equal segments. Hence, every research unit presents the stress and strain at six different temperatures. According to the Von Mises plastic yield criterion, the yield stresses of the particles and the substrate material are not related to the gas pressure, thus the yield strength can be described by the following equation (Ref 7):

$$\sigma_Y = \sigma_0 + E_p \varepsilon_{\text{eff}}^p, \quad (\text{Eq 1})$$

where  $\sigma_0$  is initial yield stress,  $\varepsilon_{\text{eff}}^p$  is effective plastic strain, and  $E_p$  is plastic hardening modulus.  $\varepsilon_{\text{eff}}^p$  and  $E_p$  can be computed by the following equations (Ref 11):

$$\varepsilon_{\text{eff}}^p = \int_0^t d\varepsilon_{\text{eff}}^p, \quad (\text{Eq 2})$$

$$E_p = \frac{E_{\text{tan}} E}{E - E_{\text{tan}}}, \quad (\text{Eq 3})$$

where  $d\varepsilon_{\text{eff}}^p = \sqrt{\frac{2}{3} d\varepsilon_{ij}^p d\varepsilon_{ij}^p}$ ,  $E$  is Young's modulus and  $E_{\text{tan}}$  is tangent modulus.

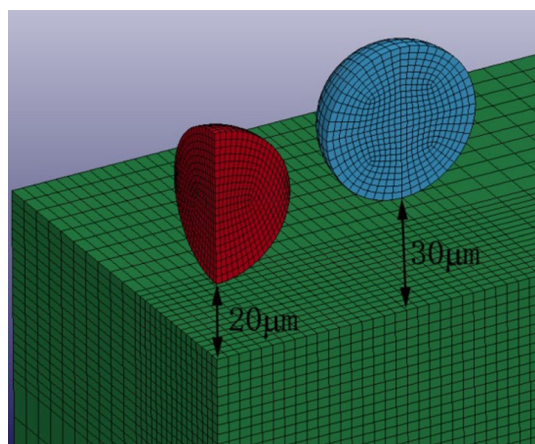


**Fig. 3** Geometric model for ANSYS Multiphysics/LS-DYNA program

**Table 4** Thermophysical parameters of mild steel used

Temperature, °C	400	850	1000	1100	1150	1200
Density, kg/m <sup>3</sup>	7850					
Poisson's ratio, $\mu$	0.33					
Young's modulus, GPa	188	118	112	100	95	90
Yield strength, MPa	350	193	119	85	71	60
Tangent modulus, MPa	500	400	305	200	183	82

**Table 5** Thermophysical parameters of St 6

Name	Density, kg/m <sup>3</sup>	Yield strength, MPa	Poisson's ratio, $\mu$	Young's modulus, GPa	Tangent modulus, MPa
St 6	8460	480	0.34	207	900

## 2.5 Numerical Computation Process and Input Parameters

For the SLD simulation, working gas is N<sub>2</sub>; gas pressure is 30 bar and gas temperature is 450 °C. Simulation parameters are given in Tables 4 and 5.

## 3. Results and Discussion

### 3.1 Deformation Behavior of Particles

The experimental parameters were used as the simulation input parameters for facilitating the comparison of the results. Figure 4 shows the effective plastic strain contours of the particle impact at four different deposition temperatures for diameter of 40  $\mu\text{m}$ . As seen in Fig. 4(a), the particles spring back at 500 °C, which may cause the deposition area (the substrate) less deformed under the reaction force of work hardening, instead, the particles exhibit large plastic deformation after impact, but smaller effective plastic strain occurs in the substrate. At this temperature, the sphere shape of the particles has changed to the shape of ellipse; while the substrate has experienced only a little plastic deformation; the impact force of the particles results in the shallowest indentation among the temperatures. Owing to the mutations of momentum of the particles, large reacting force is generated at the particle/substrate interface, which drives the particles to detach from the substrate and even leads to rebounding of the particles. During the particle impact, the hardening effect of the substrate is unavoidable because of the plastic deformation of the substrate. As a result, effective bonding is hardly formed.

Compared with Fig. 4(a), the deformation of the particles is matched with that of the substrate in the deposition zone at the temperature of 1000 °C, as shown in Fig. 4(b). This implies that good matching is formed at the interface. When the temperature rises to 1100 °C, the interface between the particle and substrate also exhibits consistent deformation with each other, but the space between the particles is not filled with the substrate material and thus the influence of the interaction between the adjacent particles cannot be neglected (Ref 27), interfaces between the particles have the zone where

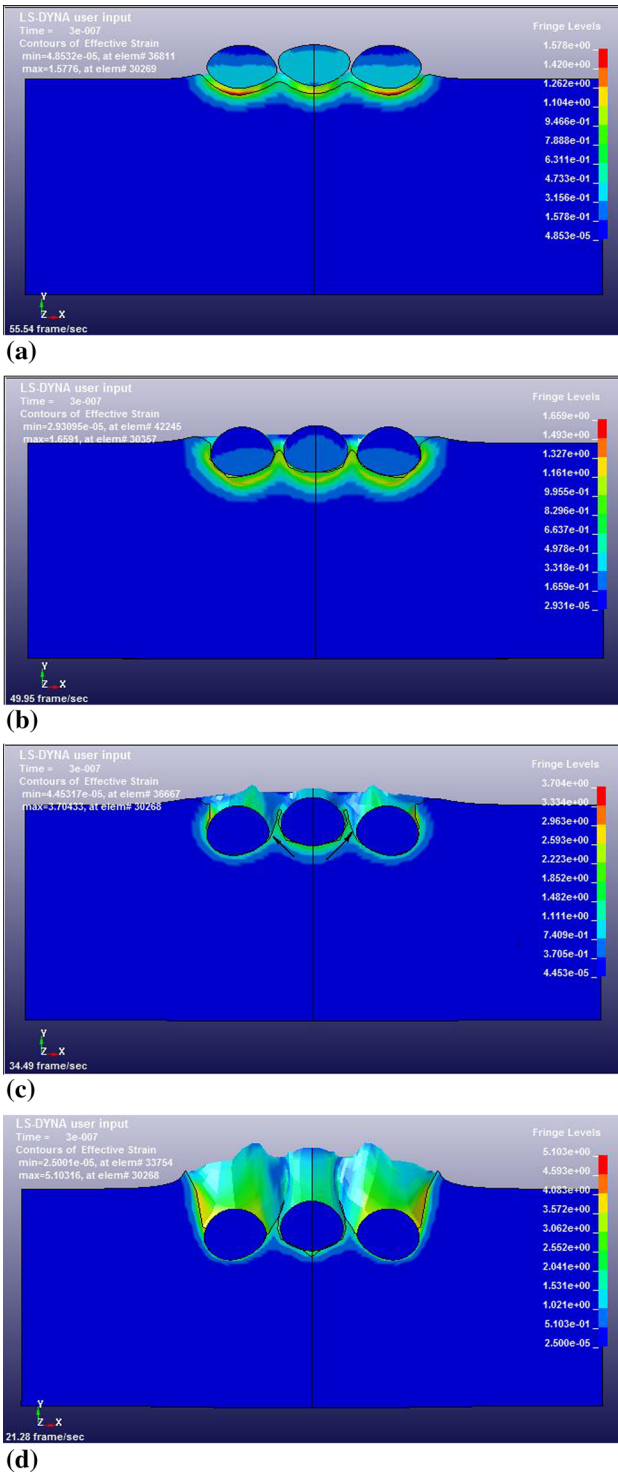


**Fig. 4** Effective plastic strain contours of the particle impacting on the substrate at different temperatures. (a) 500 °C. (b) 1000 °C. (c) 1100 °C. (d) 1200 °C

pores are found, as indicated by the arrows in Fig. 4 (c) from the simulation. In Fig. 4(d), the substrate has the highest effective plastic strain at the laser preheating temperature of 1200 °C. Due to thermal stress transfer, the effective plastic strain in the deposition zone reaches

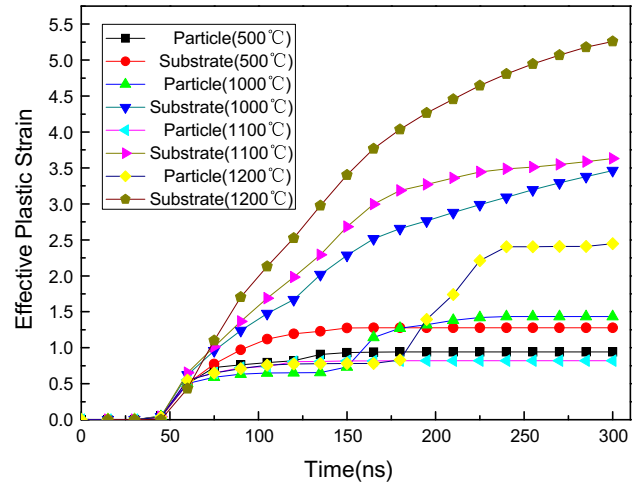


**Fig. 5** Effective plastic strains for the particles and substrate

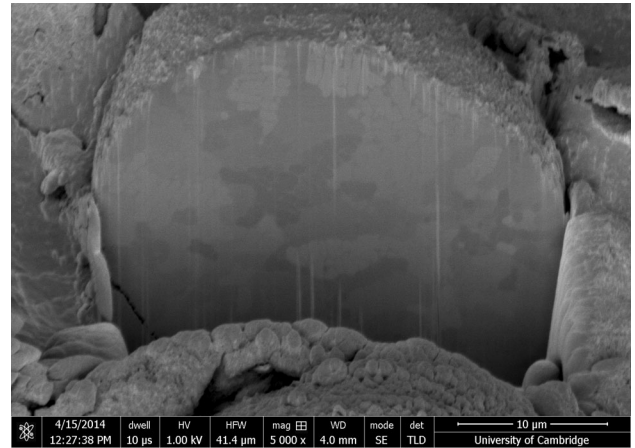
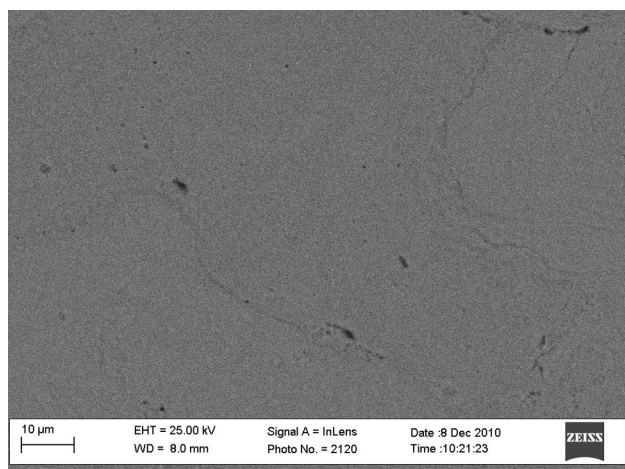


**Fig. 6** Cross-section image of single particle in SLD coating processed at 520-539 °C

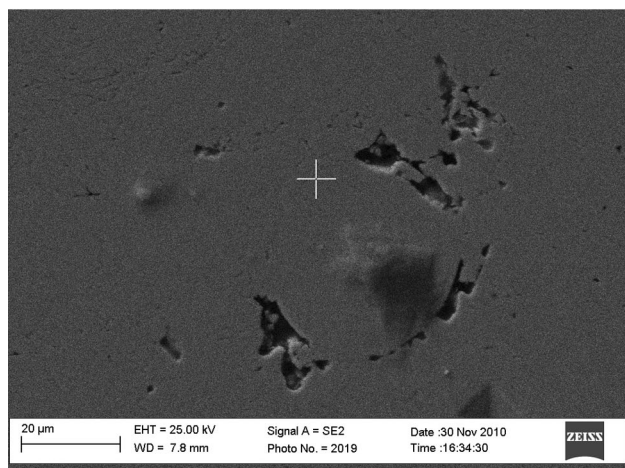
the maximum; in this case, the maximum strain that causes the maximum indentation would probably increase the coating porosity because of mismatching of strain deformation between the particle and substrate, which has detrimental effects on resisting corrosion, since the corrosive medium can reach the coating interface through the stomata and accumulate, thus causing the coating spalled off.

Figure 5 shows the effective plastic strains of the particle and substrate under particle impact at different temperatures. When the deposition temperature is 500 °C, the effective plastic strains of the particle and substrate are nearly equal before 75 ns, the subsequent effective plastic strain of the substrate is larger than that of the particles due to the fact that the particles are harder than the substrate. However, the effective plastic strain of the substrate is still very small, which causes a layer of particles rebound without subsequent particle impact it. When the deposition temperature is 1000 °C, the effective plastic strain of the substrate is larger than that of the particles. At the initial 150 ns time interval, the effective plastic

strain of the substrate increases faster than that after 150 ns. At this time, the effective plastic strain of the particles fluctuates, which indicates that the effective plastic strain of the particles does not conform with the effective plastic strain of the substrate initially and the gradual increase in the effective plastic strain of the particles allows it matching with the substrate. When the deposition temperature is 1100 °C, since the effective plastic strain of the particles would not increase with increasing of the effective plastic strain of the substrate, and the effective plastic strain of the particles becomes almost constant from 75 to 175 ns, which may result in gaps, as indicated by the arrows in the contour of Fig. 4(c).



(a)



(b)

**Fig. 7** Cross-section images of multiple track deposition SLD coating at different temperatures. (a) 1000 °C. (b) 1100 °C

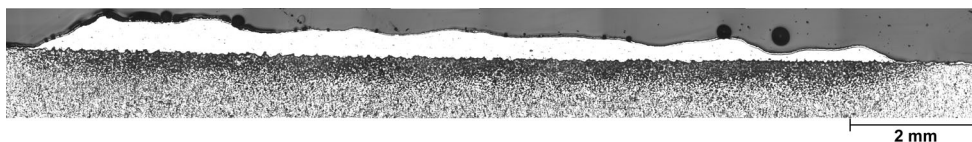


**Fig. 8** Cross-section image of multiple track deposition SLD coating processed at 1000 °C

With the particle impact proceeding, the effective plastic strain of the substrate affects the particle deformation, in other words, the variations in strain of the particle and substrate are similar, and eventually their deformations conform to each other. When the deposition temperature reaches 1200 °C, the effective plastic strain of the substrate is consistent with the particle deformation at later stage. The effective plastic strain of the substrate is very large compared with that of the particles so that the particles deposited on the substrate possibly with gaps. And cracks formed in the coating layer due to phase change at 1200 °C.

Figure 6 shows the cross section of single St 6 particle in the SLD coating processed at 520-539 °C. This image was obtained using focus ion beam (FIB), which indicates the gap between the particle and substrate in experiment comparison with simulation at 500 °C.

The simulation results at 1000 and 1100 °C was also confirmed by the deposition experiment, the cross-section images of a coating specimen processed with the same parameter as used in the simulation are shown in Fig. 7; pores are hardly found in the coating processed at 1000 °C, see Fig. 7(a). However, the optical image in Fig. 7(b) shows pores found in the coating produced at 1100 °C. As observed experimentally in Fig. 8 at 1000 °C would improve the deposition thus obtain compact coating. The cross-section image of a deposited single particle in the SLD coating processed at 1087-1137 °C was obtained using FIB, and shown in Fig. 9. It is seen that the substrate and particle are bonded strongly.

The high deposition temperature at 1200 °C causes coarse grains of martensite structure partially in the heated zone, which can initiate cracks, as observed experimentally and indicated by the arrows in Fig. 10(a). Figure 10(b) shows pores in the cross section.

Figure 11 shows the effective plastic strain contours of the particles with different particle diameters at 1000 °C. Figure 12 presents the effective plastic strains of the particles and substrate for different particle diameters at 1000 °C.

It is shown that the effective plastic strain of the particles with 25 μm is the largest within 125 ns, and then it keeps constant; while the effective plastic strain of the substrate is medium within this time interval. The smaller deformation of the substrate cannot accommodate the particles to deposit. This would result in rebound of the particles, as shown in Fig. 11(a). With increasing the particle diameter, the particles start to deposit onto the substrate. Figure 12 shows that the effective plastic strain of the substrate is larger than that of the particles with 35 μm, in other words, the slope of the substrate curve is

larger than that of the particles. In this case gaps may also form; As indicated by the arrows in Fig. 11(b). As shown in Fig. 12, among the diameters discussed, the particles with 40  $\mu\text{m}$  diameter generate larger effective plastic strain of the substrate than that of the particles within 175 ns, which benefits the particle deposition on the substrate due to smaller reaction force. After 175 ns, the variations of the effective plastic strain curves of the particles and

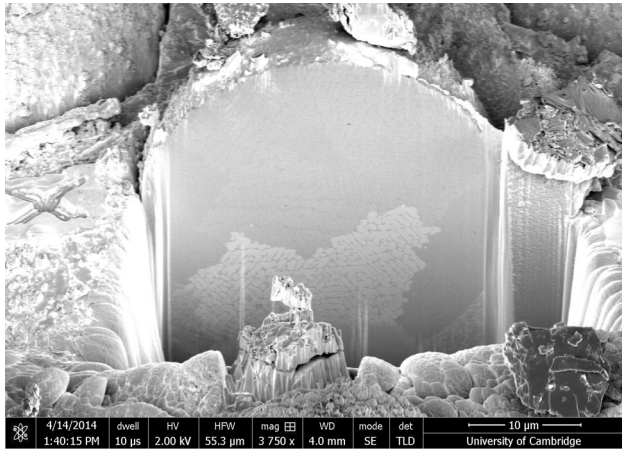


**Fig. 9** Cross-section image of single particle in the SLD coating processed at 1087-1137  $^{\circ}\text{C}$

substrate approach to the same, this implies better match of the substrate with the particles in deformation, as shown in Fig. 11(c). When the diameter of the particles is 50  $\mu\text{m}$ , the effective plastic strain of the substrate is larger than that of the particles, as presented in Fig. 11(d); hence, the bonding between the particles and substrate becomes better. However, the deformation of the particles is the least among the diameters before 175 ns, in this case, gaps may form in the bonding zone between the particles. Further deformation of the particles is induced by the heat of the bonding zone; in the meanwhile, the gap is decreased. As shown in Fig. 12, the effective plastic strains of the particles and substrate are moderate and continuous variation in this case, which reveals the strain instability during energy transmission when particle impact occurs. The simulation results with 40  $\mu\text{m}$  agree with the experimental observations for the diameter of 39.705, as shown in Fig. 1(b).

The plots in Fig. 13(a) describe the variations of indentation depth of the particles with time during the deposition process. It can be seen that the indentation depth is the shallowest at 500  $^{\circ}\text{C}$ . With increasing time all the depths increase, but at lower temperatures the indentation depths become gradually stable with time continuously increasing. The reason for this may be that the force of the particles acting on the substrate is greater than the reaction force that the substrate exerts on the particles; the substrate only experiences elastic deformation during initial stage of the particle impact. However,

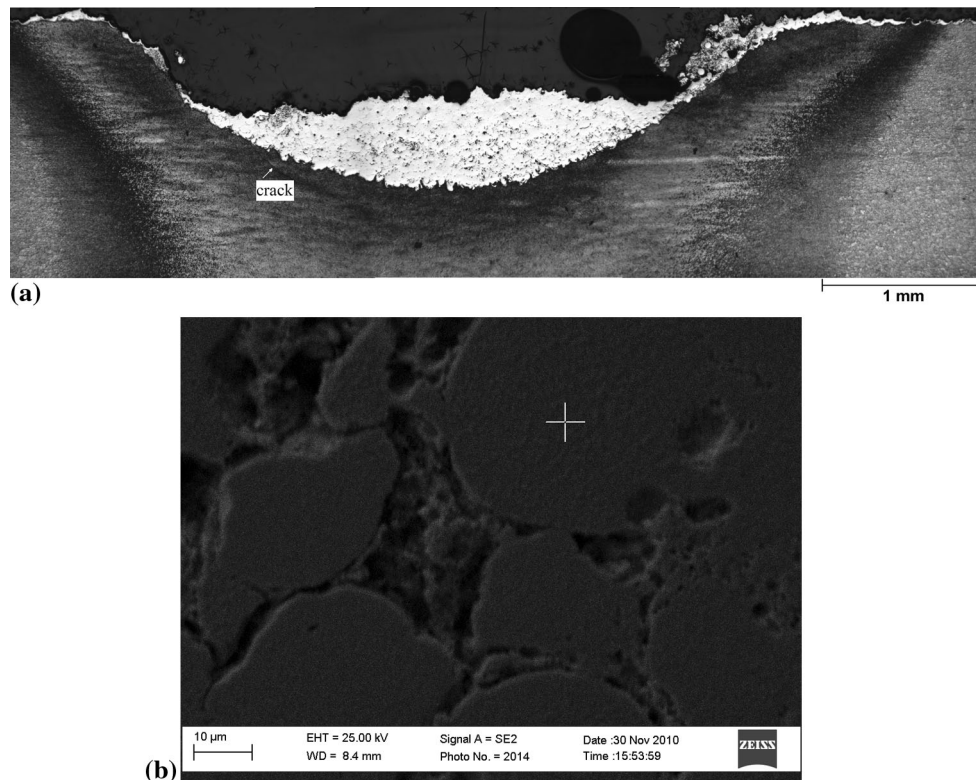
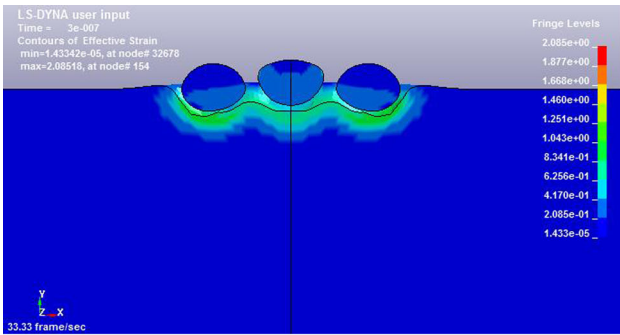
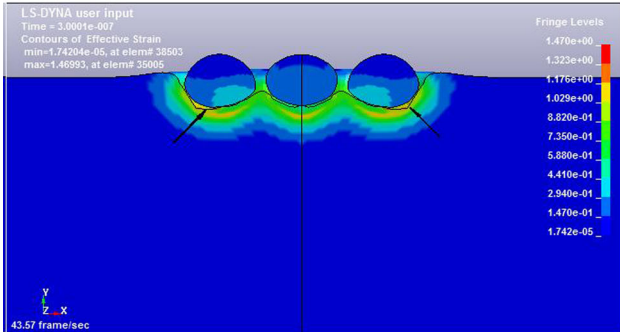


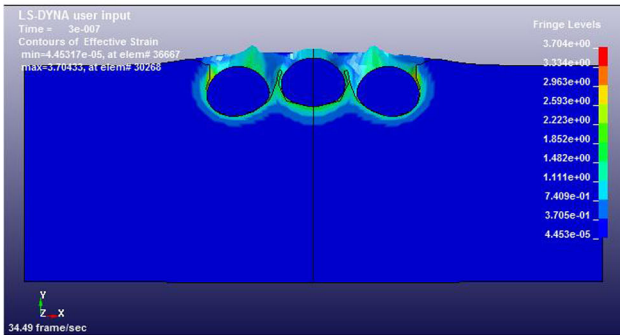
**Fig. 10** Cross-section images of multiple track deposition SLD coating at 1200  $^{\circ}\text{C}$ . (a) Cross-section. (b) coating of cross section



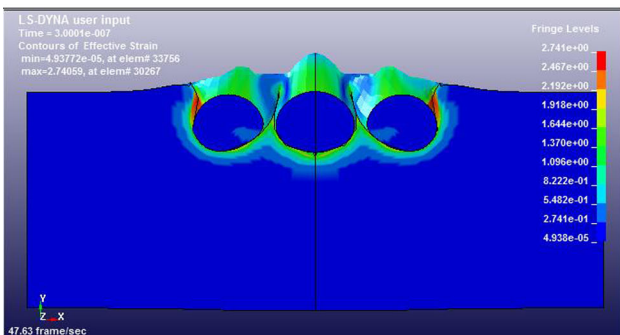
(a)



(b)



(c)



(d)

**Fig. 11** Effective plastic strain contours of particles with different diameters. (a) 25  $\mu\text{m}$ . (b) 35  $\mu\text{m}$ . (c) 40  $\mu\text{m}$ . (d) 50  $\mu\text{m}$

the indentation depth significantly increases with time when the deposition temperature reaches 1000  $^{\circ}\text{C}$ . This is because the heated substrate has beneficial effects on

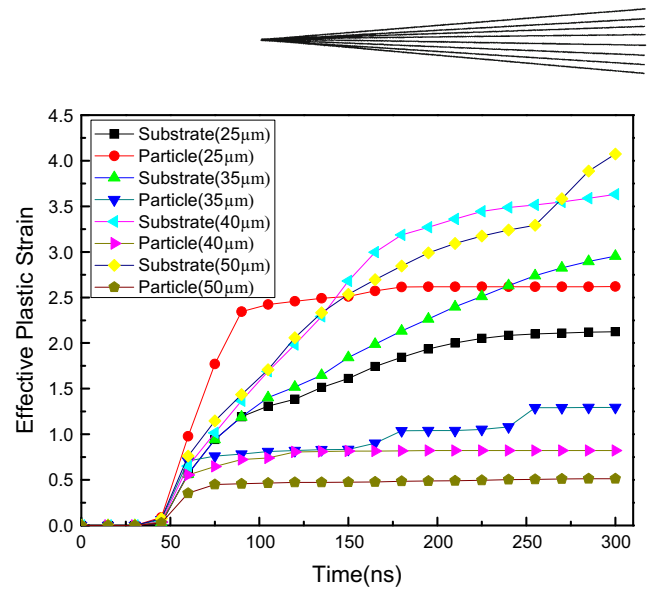
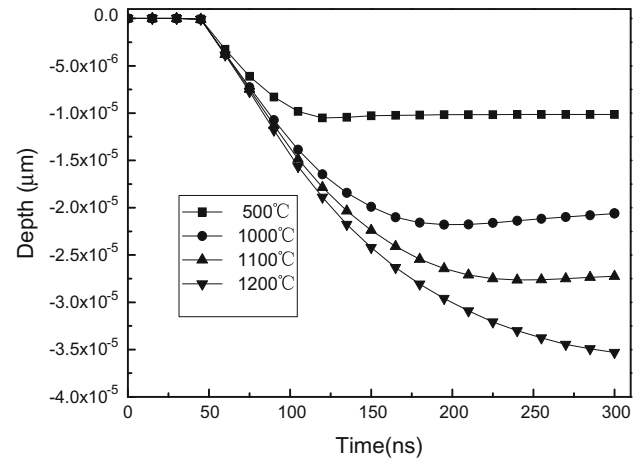
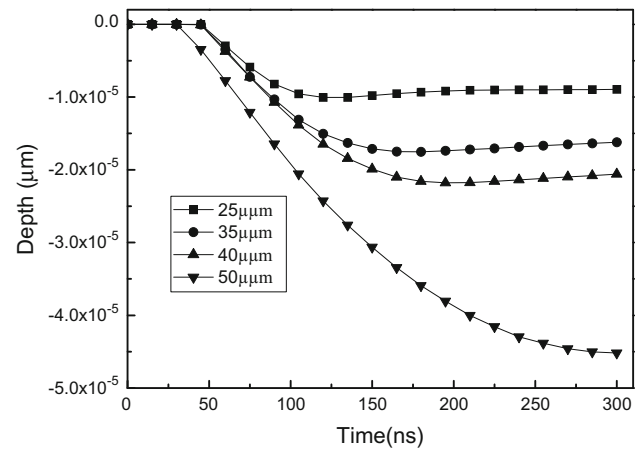


**Fig. 12** Effective plastic strains of particles and substrate for different particle diameters



**(a)** Indentation depths for different process temperatures



**(b)** Indentation depths for different particle diameters

**Fig. 13** Indentation depth vs. particle impact time



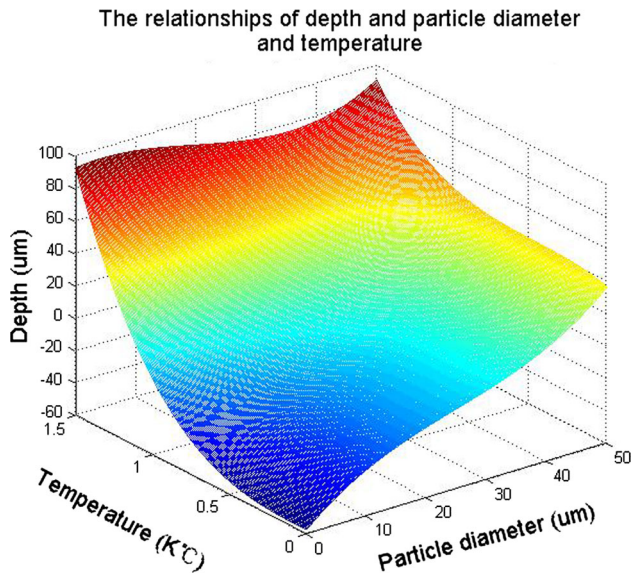


**Fig. 14** Relationships between the substrate temperature, particle diameter and indentation depth

promoting the particle penetration into the substrate thus increasing the indentation depth. This phenomenon is mainly due to the plastic deformation of the substrate. Nevertheless, when the deposition temperature reaches 1200 °C, the substrate material (carbon steel) has changed from the ferrite and pearlite phases to martensite, which results in cracking of the material.

Figure 13(b) presents the simulation results of indentation depth variation with particle diameter. It is found that the collision and depth increase greatly with the increase of the particle diameter. The largest increase rate of the indentation depth is observed for the particle diameter of 50 μm. The reason for this behavior is attributed to the fact that the kinetic energy of the particles with 50 μm when impacting on the substrate is the largest, from Eq 4 below, thus leading to the depth increase. However, for other particle diameters, the indentation depth becomes unchanged after a certain period of impact time. In cold spray, it is the high kinetic energy of the particle that ensures sufficient deformation of the substrate material on impact. The kinetic energy of a particle can be determined by

$$KE = 1/2 mv^2, \quad (\text{Eq 4})$$

where  $m$  and  $v$  are mass and velocity of the particles, respectively;  $m$  is dependent on  $d^3$  where  $d$  is diameter of the particles. It is clear that there will always be a trade-off between  $d^3$  and  $v^2$ . In cold spray, the particle bonding on the substrate is dependent on if the particle reaches its  $V_{\text{crit}}$  upon impact. For larger particles,  $V_{\text{crit}}$  is lower, but it takes longer time to accelerate them sufficiently, as reported by Schmidt et al. (Ref 28). In their model, a simple relationship was found between the particle size and velocity required for deposition:  $V_{\text{crit}} = 900 d^{-0.19}$  for copper and  $V_{\text{crit}} = 950 d^{-0.14}$  for stainless steel (316L). They also suggested the optimum particle size range of

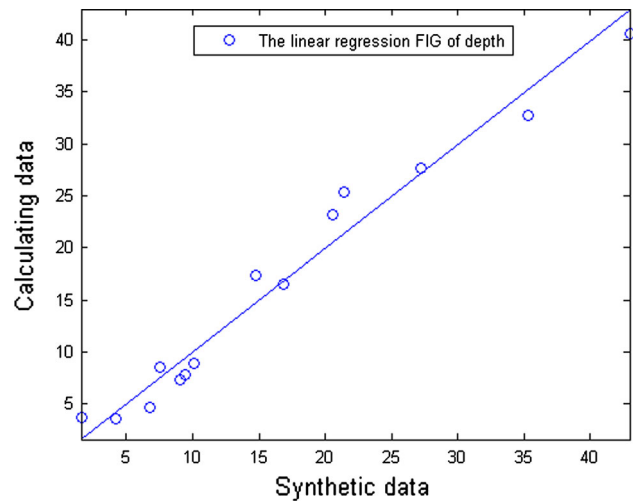


**Fig. 15** Linear regression diagram for the indentation depth

–45 + 10 μm for cold spray deposition. The effect of particle size on the critical velocity for titanium particles (at different temperatures) impacting on a titanium substrate was investigated experimentally and numerically by Kuroda et al. (Ref 18). As particle size was increased, the critical velocity decreased, which indicated that bigger particles were easier to adhere to the substrate with the same impacting velocity. In the present research, the deposition zone was heated by laser; therefore, the indentation of bigger particles is deeper at the same impact velocity.

Based on the indentation depth results in Fig. 13, using the Matlab software, the relation equation can be obtained by fitting the simulation data, as expressed by Eq 5 and illustrated in Fig. 14, where,  $Y_1$  is indentation depth,  $X_1$  is particle diameter,  $X_2$  is deposition temperature

$$Y_1 = -57.6159 + 3.3594X_1 - 0.0898X_1^2 + 0.0123X_1^2X_2 - 1.2575X_1X_2^2 + 0.0012X_1^3 + 44.3897X_2^3. \quad (\text{Eq 5})$$

It can be seen that the indentation depth increases with the particle diameter when the temperature remains constant. On the other hand, when the particle diameter is constant, the indentation depth increases with the temperature. In addition, when the particle diameter and indentation depth are known, the other variable, deposition temperature, can be estimated from Eq 5. The results (the relation equation and simulation data) can provide the reference data for the experiment of St 6 alloy particles deposited on the steel and determine reasonable process parameters for this alloy that can be used in the actual operation.

Figure 15 provides the linear regression diagram of the indentation depth by fitting the simulation and calculation results of Eq 5. The straight line is the linear regression fitted by the calculation and simulation values, while the spots represent the calculation and simulation values. The

closer the spots to the line of the linear regression, the more accurate of the simulation and calculation results of the depth are. According to the fitness of the data in Fig. 15, the accuracy of Eq 5 is high.

### 3.2 Deformation Characteristics of the Particles with Optimized Parameters

**3.2.1 Three-Particle Impact Simulation.** Previous experimental studies of St 6 deposited on steel substrate by SLD were reported (Ref 23), but the deformation characteristics of the adjacent particles during St 6 particle impacting on steel were not studied. The simulation was based on the fact that the adjacent particles must be involved in deformation and bound with each other during the SLD process. When the particles are impacting on the substrate, high impact velocity and deformation occur, which may not be observed directly in the real deposition process, but the deformation process and the bonding between two particles in multi-particles or between the particle and the substrate as “unit process” can be

simulated, together with the stress-strain behavior between two particles, and between the particle and the substrate. Figure 16 illustrates the three-particle impacting model for the particle diameter of 40  $\mu\text{m}$ , distance of 10  $\mu\text{m}$  between contact surfaces of the particles (Ref 27). The process parameters have been experimentally optimized, given in Table 3; they are impact velocity of 450 m/s and laser power of 1.5 kW at deposition temperature of 1000  $^{\circ}\text{C}$ .

Figure 17 shows the deformation characteristics of the three particles of St 6 at different times. The particles impact on the heated steel substrate at the initial velocity of 450 m/s. Suppose that particle A impacts on the substrate first at 75 ns, particle B and particle C follow, which results in mild plastic flow between the substrate and particles. At 120 ns, the violent plastic deformations of the particles and substrate change sphere particle into spheroidicity, and much high temperature on the soft side of the heated steel substrate deforms obviously with “jet”, as indicated by arrows in Fig. 17. Impact morphology is

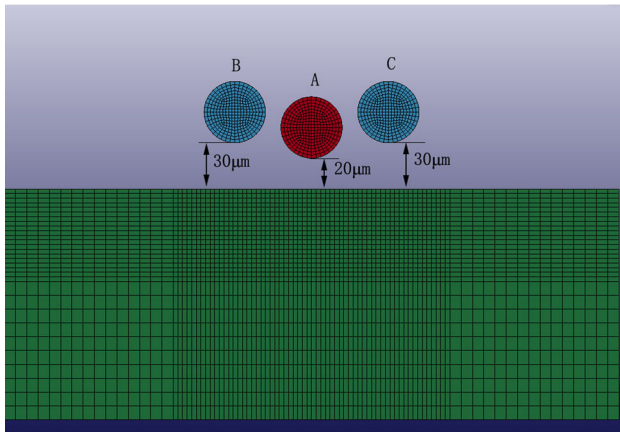


Fig. 16 Three-particle impacting model

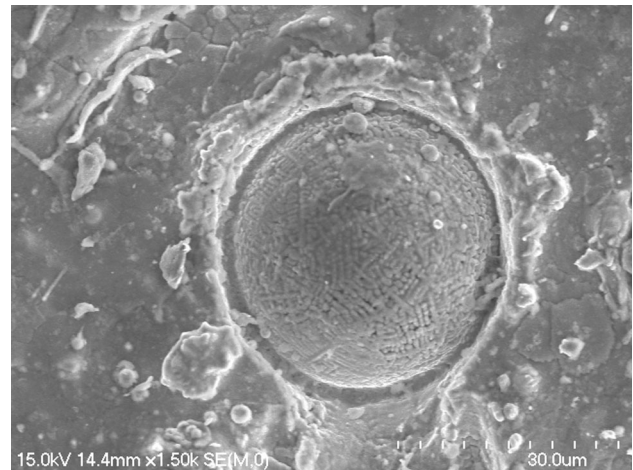


Fig. 18 Impact morphology for single particle

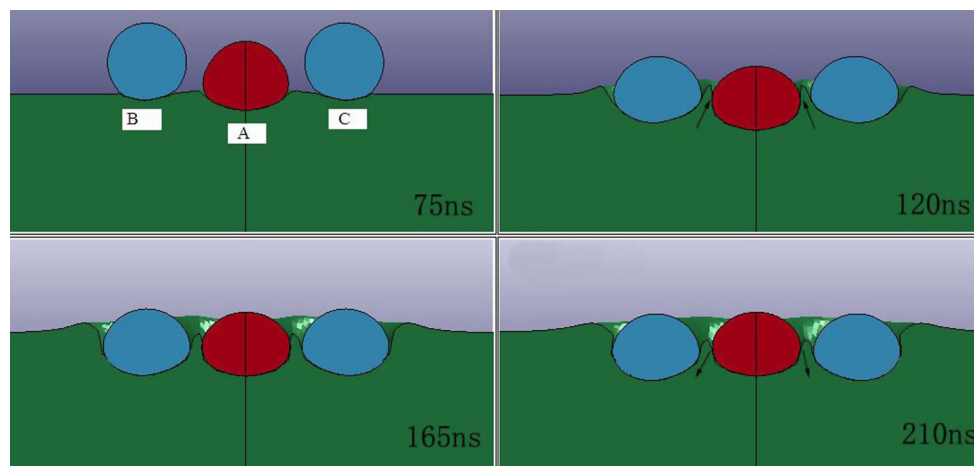
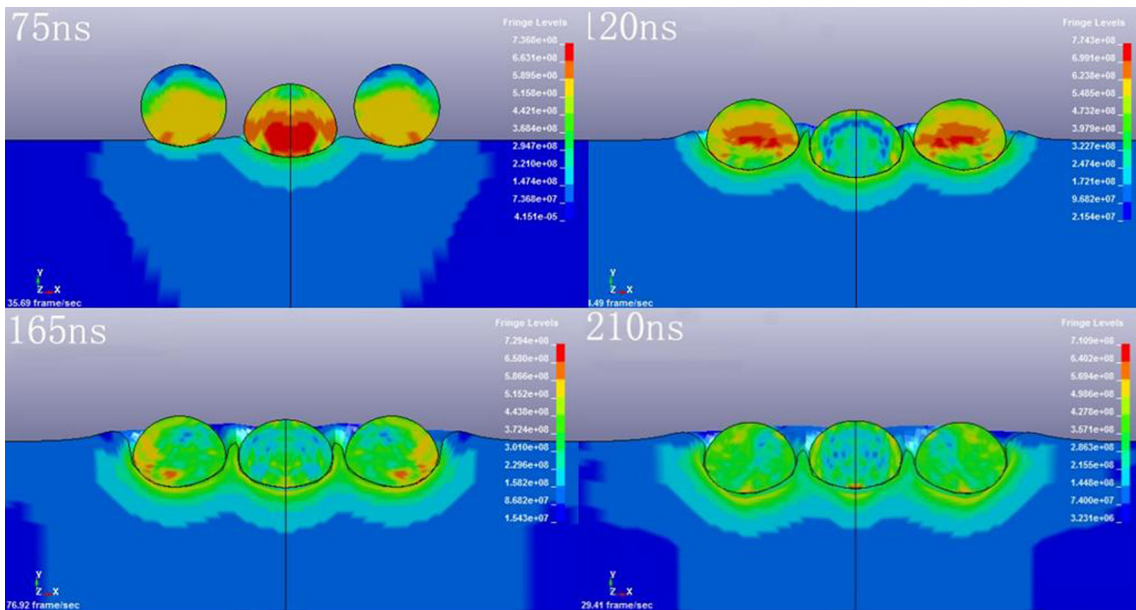
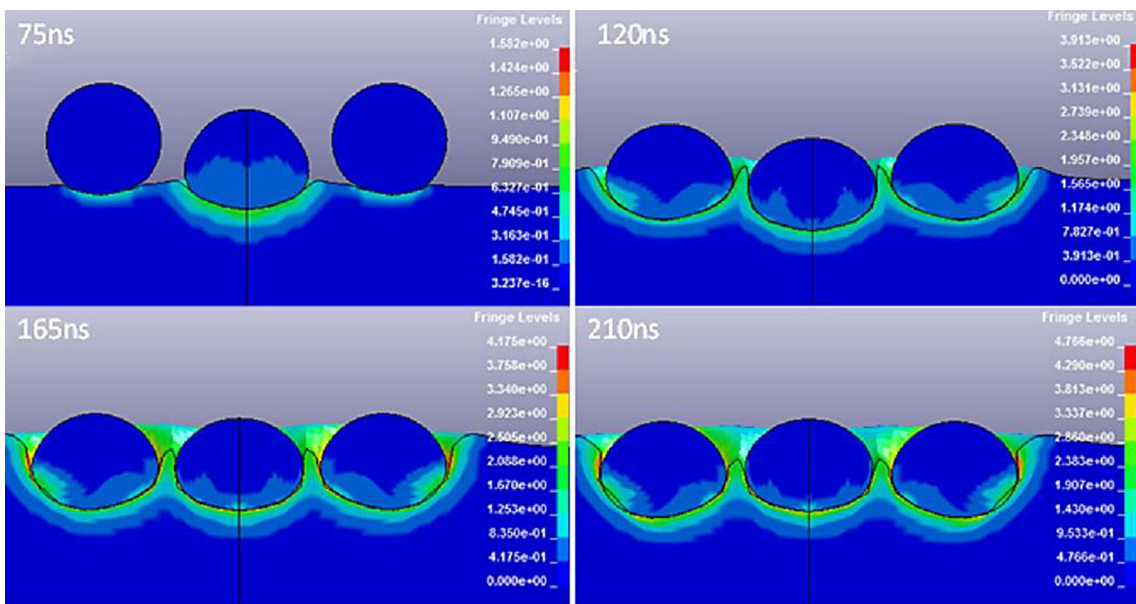


Fig. 17 Impact characteristics of the particles at different times



**Fig. 19** Effective plastic stress distributions at different times of particle impact



**Fig. 20** Effective plastic strain distributions at different times of particle impact

shown in Fig. 18. The “jet” of the substrate, to a great extent, increases the contact area and effective bonding between particle A and the substrate. An important reason to concern the “jet” possibly is to understand the interaction between the particles or harder particle impact on the heated soft substrate (Ref 29). When particle A impacts on the substrate, the high impact force makes the heated substrate material deform. The impacts of particles B and C prevent particle A from forming plastic flow. As a result, the interaction time for particle A is too short to induce plastic flow around it completely, thus the plastic

flow moves to the gap between the particles and encircles most of particle A.

In the meanwhile, particle A is extruded by particles B and C. With increasing the impact time, particles B and C start to deform plastically with the shape change from sphere to spheroidicity, the plastic flow of the substrate that causes pressure to the left and right sides of particle A, creates mechanical bond between the particle and substrate, holding particle A from rebounding. After 165 ns, particle A almost stops moving maybe due to the interaction between particles B and C or the kinetic

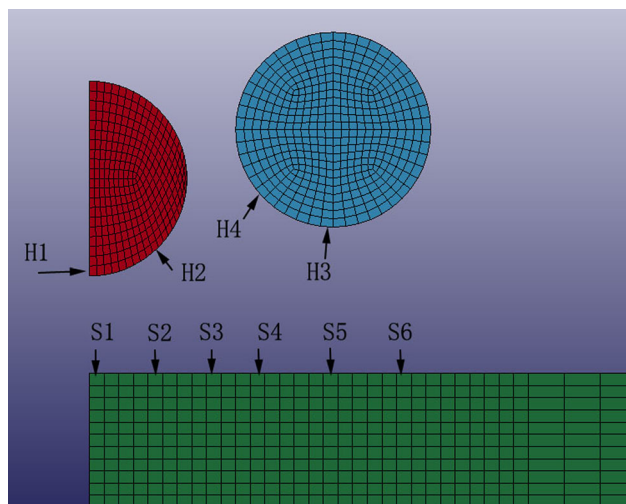
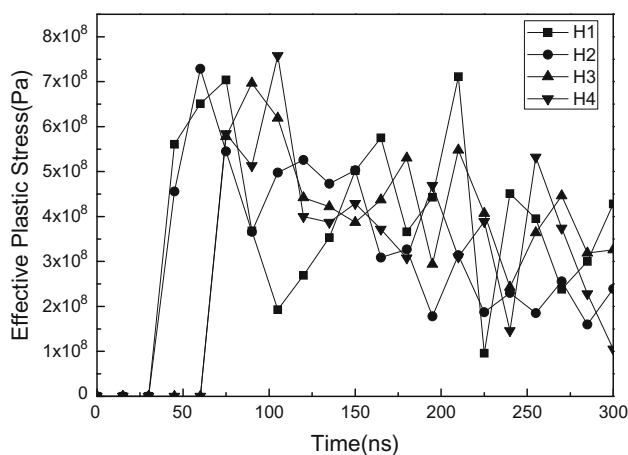
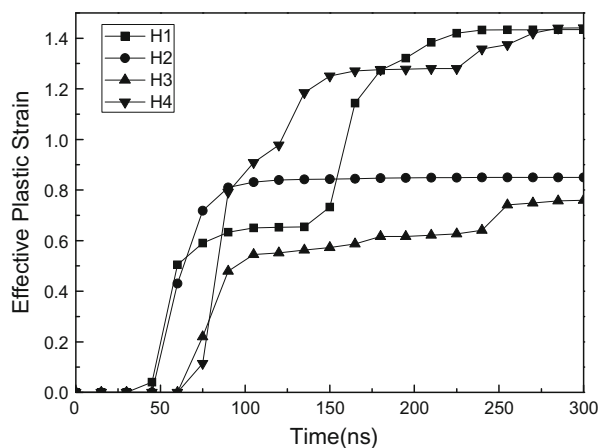


**Fig. 21** Sketch of micro-zone for the particles and substrate



**(a)** Effective plastic stress



**(b)** Effective plastic strain

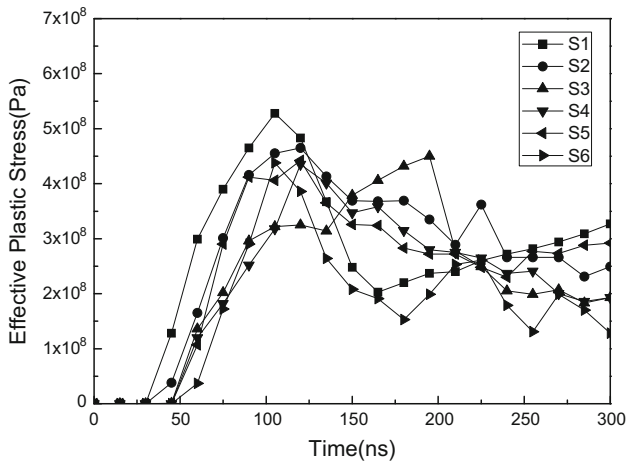
**Fig. 22** Effective plastic stress and strain variations of the particles with time

energy of the particle A disappear, but particles B and C still move continuously to the inside of the substrate, on the one hand they are at the edge of deposition zone, where is free of particle pressure except the pressure from the substrate. On the other hand, their kinetic energies still exist at that moment, which causes plastic flow (jet) around particle A. In addition, after 120 ns, the deformation of the particles almost does not occur with the impact continuing. This may be attributed to the heated substrate, which increases the substrate plastic deformation. This behavior implies that the limited plasticity of the particles and the lower reactive force from the substrate do not allow the particles to deform continuously. Also, the stress at the impact interface is too small to allow the particles inducing larger deformation. The substrate almost absorbs whole kinetic energy of the particles, consequently effective bonding is formed at the particle/substrate interface, so as to reduce interspace between the particles and substrate and produce a compact coating.

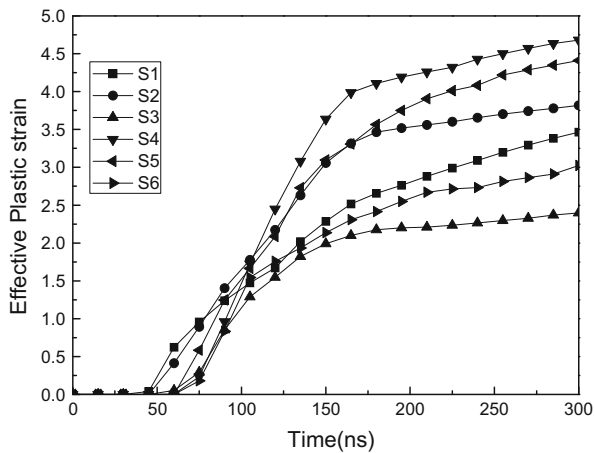
**3.2.2 Stress-Strain Behavior of the Particles.** The effective plastic stress and strain distributions at different times of particle impact are illustrated in Fig. 19 and 20, respectively. It is evident that the particles are stretched to a shape of ellipsoid from sphere gradually; its height to width ratio is decreased so that the contact area between the particles and substrate is increased continuously. Thus, the size of deposition indentation increases with the impact time. At 75 ns, the highest stress is mostly concentrated at the edge of impact interface at the instant of the particle impacting on the substrate. During the initial stage of impact, the change of the stress is irregular due to the interaction between the particles and substrate. As seen in Fig. 20, the effective plastic strain is uniformly distributed at the interface between the particles and substrate; the effective plastic strain of the particles is less than that of the substrate. The effective plastic strain of the substrate is concentrated in the interface layer of the deposition indentation. For particles, the effective plastic strain is limited in a small area between the particles and substrate.

In order to further understand the effect of the collisional behavior of multi-particles on the stress-strain distributions, consider a typical micro-area in the particle and substrate system, such as the centre of impacts H1 and H3 and the edges of contact zone H2 and H4, as shown in Fig. 21. Particle A is related to H1 and H2; Particle B H3 and H4; the contact zones between the substrate and particle A or between the substrate and particle C are S1, S2, S4, S5, S6, respectively. S3 is a micro-contact zone between two particles impacting on the substrate. The simulation results are presented in Fig. 22 and 23.

As shown in Fig. 22(a), the effective plastic and stress curves have violent fluctuation; the biggest peak of the stress for the particles appears on H2-curve and H4-curve. In Fig. 22(b), the strains increase with time, and the strains of H1 area and H3 area are smaller than those of H2 area and H4 area in the initial time period. However, after 150 ns, the strain of H1 area increases rapidly due to the interaction of adjacent particles or with the substrate.



(a) Effective plastic stress of the substrate



(b) Effective plastic strain of the substrate

**Fig. 23** Effective plastic stress and strain variations of the substrate with time. (a) Effective plastic stress. (b) Effective plastic strain

Particle A is subjected to the reaction force from the substrate; therefore, the curves of the stress and strain of particle A show obvious jumping. Particle C, due to less pressure from adjacent particles and larger distance from the interface, its stress and the strain curves do not exhibit the same jumping compared with particle A. In fact, the coating deposition is a very complex process and it is a function of various possible mechanical properties of the particles; not all of these have been yet fully understood.

The stress and strain curves of the substrate show less fluctuation compared to those of the particles. This may be due to the fact that the thermally (by laser) softened substrate loses its ability to store elastic energy (Ref 28), which can be seen in Fig. 23. Compared with the curves in Fig. 22, the stresses of the substrate are lower than those of the particles; and the strains are larger than those of the particles. This can also be explained as the deformation of the substrate is larger than that of the particles.

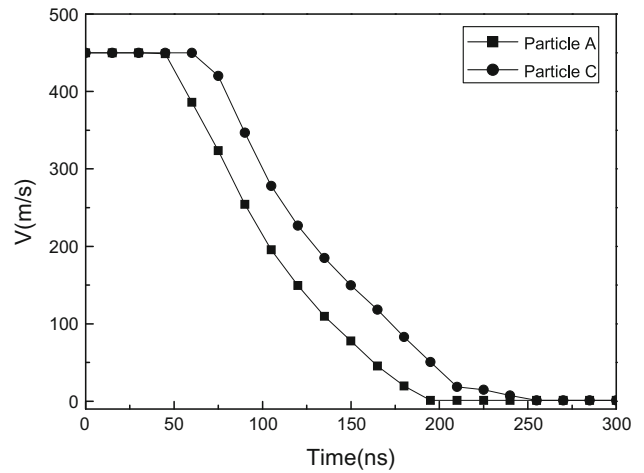


**Fig. 24** Variations of the particle velocity with time

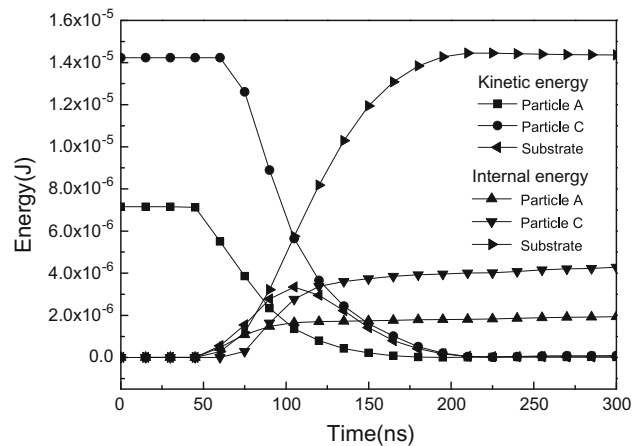
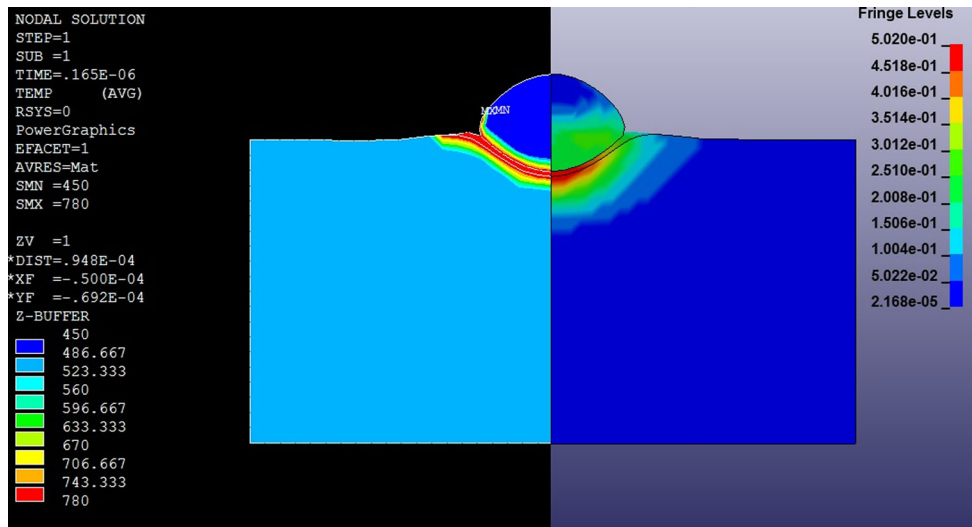
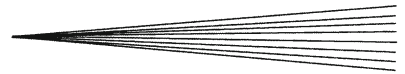


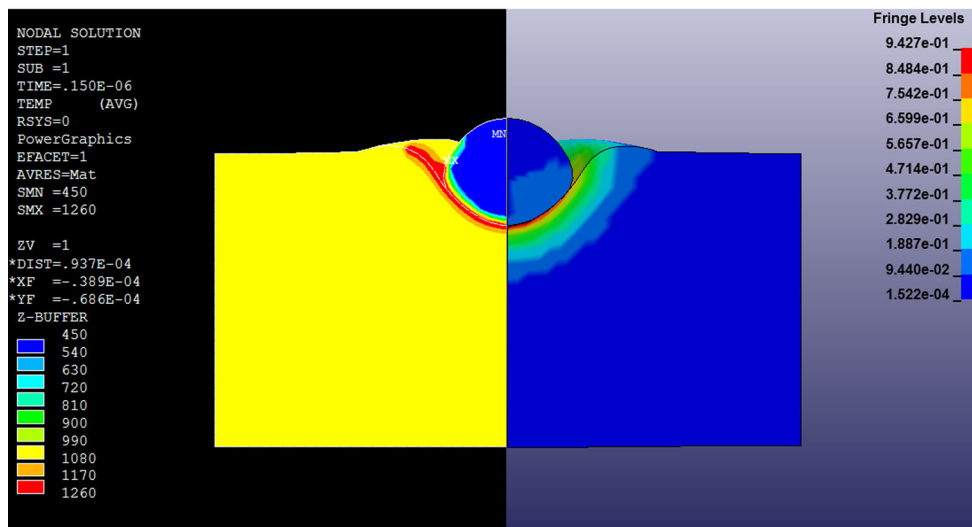
**Fig. 25** Variations of the energies of the particles and substrate with time

### 3.3 Energy and Velocity of Multi-particle Impact

During St 6 particle impacting on steel substrate, whatever the particles or the substrate experience the changes of velocity and energy. As shown in Fig. 24, before 50 ns, the impact velocity of the particles stays at a constant level, after 50 ns, the impact velocity decreases linearly with time; at 200 ns it becomes constant again. This indicates that the initial kinetic energy is converted to mechanical energy, leading to mechanical bond between the particles and substrate. This can also be proven from the curves in Fig. 25. At 50 ns, the kinetic energy of particle A is higher than that of particle C, and the internal energies of the particles and substrate are zero, while between 50 and 200 ns, the energies of both particles and substrate increase with time, and the latter increases more rapidly and reaches a value of  $1.4 \times 10^{-5}$  J. After 200 ns, however, it tends to a constant level. The kinetic energies of the particles and substrate decrease to zero eventually.



(a) Deposition temperature at 500°C



(b) Deposition temperature at 1000°C

**Fig. 26** Contours of the temperature and effective plastic strain for single St 6 particle deposited on steel with different substrate temperatures

From 50 ns to 100 ns, the kinetic energy of the substrate increases and then decreases to zero at 200 ns.

### 3.4 Temperature Contours and Effective Plastic Strain for Single Particle

In order to compensate the deficiency of Johnson-Cook model in missing some important aspects, the temperatures of 500 and 1000 °C are applied on the simple model unit after plastic deformation, thus to obtain the temperature contours and the effective plastic strain for single particle, as shown in Fig. 26. It can be seen that highest temperature in the contours is higher than that of preset. This is because the particle impact results in energy of the plastic strain and the impact friction would improve the

interface temperature between the particle and the substrate. The conversation of energy during the particle impact can be simply described by the following equation:

$$E_U = E_P + E_V + E_F + E_R,$$

where  $E_U$  is initial kinetic energy,  $E_P$  is plastic dissipation energy,  $E_V$  is viscous dissipation energy, and  $E_F$  is frictional dissipation energy.

According to the energy balance concept, adiabatic local heating at interface induced by the plastic dissipation energy and the viscous/frictional dissipation energy contributes to “adhesion energy”, and only the stored elastic strain energy can be recovered as “rebound energy” (Ref 30). Therefore, when the plastic dissipation

energy and the viscous/frictional dissipation energy during impact are greater than “rebound energy”, the particles can be deposited on the substrate, as seen in Fig. 9; otherwise, the particles rebound, as shown in Fig. 6.

The deposition characteristics in terms of energy can be described by the curves in Fig. 25. The effective plastic strain energy of single particle is lower than that of multi-particles; this may be due to the fact that the interaction between particles for multi-particles results in increasing of the effective plastic strain.

## 4. Conclusions

- (1) Laser deposition temperature and particle size for St 6 particles deposited on mild steel substrate were optimized with respect to the interface bonding. The deposition temperature of 1000 °C and St 6 particle size of 40 μm exhibit the best deposition behavior. The simulation results conformed to the experimentally optimized parameters: the deposition temperature of 1000 °C, the particle diameter (0.5) of 39.705 μm.
- (2) The depths of impact indentation for different St 6 particle sizes and different temperatures were investigated, and the relation equation was obtained for St 6 between particle diameter, indentation depth, and the deposition temperature using Matlab software, as follows:

$$Y_1 = -57.6159 + 3.3594X_1 - 0.0898X_1^2 + 0.0123X_1^2X_2 - 1.2575X_1X_2^2 + 0.0012X_1^3 + 44.3897X_2^3$$

The results (the relation equation and simulation data) can provide the reference data for St 6 particles deposited on steel and determine reasonable process parameters for actual operation.

- (3) The effective plastic stress and strain of the micro-zone for St 6 particles impacting on mild steel was investigated using FEA modeling. The results show that heated steel substrate by laser benefits the deposition of St 6 particles because of the enhanced plastic deformation of the substrate in the deposition zone. The limited plasticity of the particles and the lower reactive force from the substrate do not allow the particles to deform continuously, and also the stress at the impact interface is too low to cause the plastic deformation of the particles. As a result, the substrate almost absorbs whole kinetic energy of the particles, thus effective bonding at the particle/substrate interface can be formed, so as to decrease interspace between the particles and substrate and form a compact coating.

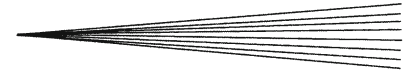
## Acknowledgments

This project is sponsored by the Natural Science Foundation of China (51271170). China International Science and Technology Cooperation Project (2012C

11001). The authors wish to express their gratitude to Mr. Bing Zhao for providing assistance in simulation.

## References

1. A.S.M. Ang, C.C. Berndt, and P. Cheang, Deposition Effects of WC Particle Size on Cold Sprayed WC-Co Coatings, *Surf. Coat. Technol.*, 2011, **205**, p 3260-3267
2. R. Lupoi, M. Sparkes, A. Cockburn, and W. O'Neill, High Speed Titanium Coatings by Supersonic Laser Deposition, *Mater. Lett.*, 2011, **65**, p 3205-3207
3. R. Lupoi, A. Cockburn, C. Bryan, M. Sparks, F. Luo, and W. O'Neill, Hard-Facing Steel with Nanostructured Laser Deposition, *Light Sci. Appl.*, 2012, **1**, p e10. doi:10.1038/lssa.2012.10. www.nature.com/lssa
4. M. Kulmala and P. Vuoristo, Influence of Process Condition in Laser-Assisted Low-Pressure Cold Spraying, *Surf. Coat. Technol.*, 2008, **202**(18), p 4503-4508
5. N. Cinca, M. Barbosa, S. Dosta, and J.M. Guilemany, Study of Ti Deposition onto Al Alloy by Cold Gas Spraying, *Surf. Coat. Technol.*, 2010, **61**(11), p 1096-1102
6. B.N. Mordyuk, V.V. Silberschmidt, G.I. Prokopenko, Yu.V. Nesterenko, and M.O. Iefimov, Ti Particle-Reinforced Surface Layers in Al: Effect of Particle Size on Microstructure, Hardness and Wear, *Mater. Charact.*, 2010, **61**(11), p 1126-1134
7. Z. Xianglin, S. Xianyong et al., Simulation Effect of Cold-Sprayed Particles Properties on Their Impacting Behaviors, *Acta Metall. Sin.*, 2008, **44**(11), p 1286-1291
8. W.-Y. Li, H. Liao, C.-J. Li, G. Li, C. Coddet, and X. Wang, On High Velocity Impact of Micro-sized Metallic Particles in Cold Spraying, *Appl. Surf. Sci.*, 2006, **253**, p 2852-2862
9. M. Grujicic, C.L. Zhao, W.S. DeRosset, and D. Helfrich, Adiabatic Shear Instability Based Mechanism for Particles/Substrate Bonding in the Cold-Gas Dynamic-Spray Process, *Mater. Des.*, 2004, **25**, p 681-688
10. H. Assadi, F. Gärtner, T. Stoltenhoff, and H. Kreye, Bonding Mechanism in Cold Gas Spraying, *Acta Mater.*, 2003, **51**(15), p 4379-4394
11. T. Stoltenhoff, H. Kreye, and H.J. Richter, An Analysis of the Cold Spray Process and its Coatings, *J. Therm. Spray Technol.*, 2002, **11**, p 542-550
12. S.V. Klinkov, V.F. Kosarev, and M. Rein, Cold Spray Deposition: Significance of Particle Impact Phenomena, *Aerosp. Sci. Technol.*, 2005, **9**, p 582-591
13. J.P. Andrew, Experiment on Impact, *Phys. Soc.*, 1930, **43**, p 8-17
14. J.W. Wu, H.-Y. Fang, S.-H. Yoon, H.-J. Kim, and C.-H. Lee, Measurement of Particle Velocity and Characterization of Deposition in Aluminum Alloy Kinetic Spraying Process, *Appl. Surf. Sci.*, 2005, **252**, p 1368-1377
15. J.-H. Lee, S.-M. Shin, H.-J. Kim, and C.-H. Lee, Effect of Gas Temperature on Critical Velocity and Deposition Characteristics in Kinetic Spraying, *Appl. Surf. Sci.*, 2007, **253**, p 3512-3520
16. X.-J. Ning, J.-H. Jang, and H.-J. Kim, The Effects of Powder Properties on In-flight Particle Velocity and Deposition Process During Low Pressure Cold Spray Process, *Appl. Surf. Sci.*, 2007, **253**, p 7449-7455
17. Y. Danlos, S. Costil, X. Guo, H. Liao, and C. Coddet, Ablation Laser and Heating Laser Combined to Cold Spraying, *Surf. Coat. Technol.*, 2010, **205**, p 1055-1059
18. S. Kuroda, J. Kawakita, M. Watanabe, and H. Katanoda, Warm Spraying—A Novel Coating Process Based on High-Velocity Impact of Solid Particles, *Sci. Technol. Adv. Mater.*, 2008, **9**, p 1-17
19. S. Yin, X. Wang, X. Suo, H. Liao, Z. Guo, W. Li, and C. Coddet, Deposition Behavior of Thermally Softened Copper Particles in Cold Spraying, *Acta Mater.*, 2013, **61**, p 5105-5118
20. M. Yu, W.-Y. Li, F.F. Wang, X.K. Suo, and H.L. Liao, Effect of Particle and Substrate Preheating on Particle Deformation Behavior in Cold Spraying, *Surf. Coat. Technol.*, 2013, **220**, p 174-178
21. P.C. King, C. Busch, T. Kittel-Sherri, M. Jahedi, and S. Gulizia, Interface Melding in Cold Spray Titanium Particle Impact, *Surf. Coat. Technol.*, 2014, **239**, p 191-199



22. P.C. King and M. Jahedi, Relationship Between Particle Size and Deformation in the Cold Spray Process, *Appl. Surf. Sci.*, 2010, **256**, p 1735-1738
23. F. Luo, A. Cockburn, R. Lupoi, M. Sparkes, and W. O'Neill, *Surf. Coat. Technol.*, 2012, **212**, p 119-127
24. H. Hu, M. Yang, and D. Zhang, (*ANSYS10.0*) *A Tutorial in Finite Element Analysis for the Material Engineering*, Publishing House of Electronics Industry, Beijing, 2008 (in Chinese)
25. T. He, J. Yang, and X. Jin, *A Tutorial of ANSYS10.0/LS-DYNA Nonlinear Finite Element Analysis*, Machinery Industry Press, Beijing, 2007 (in Chinese)
26. S. Yin, X. Wang, B.P. Xu, and W. Li, Examination on the Calculation Method for Modeling the Multi-particle Impacting Process in Cold Spraying, *J. Therm. Spray Technol.*, 2010, **19**(5), p 1032-1041
27. S. Yin, X. Wang, W. Li, and B. Xu, Numerical Investigation on Effects of Interactions Between Particles on Coating Formation in Cold Spraying, *J. Therm. Spray Technol.*, 2009, **18**(4), p 686-693
28. T. Schmidt, F. Gartner, H. Assadi, and H. Kreye, Development of a Generalised Parameter Window for Cold Spray Deposition, *Acta Mater.*, 2006, **54**, p 729-742
29. J.F. Molinari and M. Ortiz, A Study of Solid-Particle Erosion of Metallic Targets, *Int. J. Impact Eng.*, 2002, **27**, p 347-358
30. G. Bae, Y. Xiong, S. Kumar, K. Kang, and C. Lee, General Aspects of Interface Bonding in Kinetic Sprayed Coatings, *Acta Mater.*, 2008, **56**, p 4858-4868